# Supplementary Information

**Pattern-assisted stacking colloidal quantum dots for photonic integrated circuits**

Kexiu Rong[a], Hui Liu[a], Kebin Shi[a,b,c] and Jianjun Chen*[a,b,c]

*Corresponding Author: E-mail: jjchern@pku.edu.cn

[a.] State Key Laboratory for Mesoscopic Physics, School of Physics, Peking University, Beijing, 100871, China
[b.] Nano-optoelectronics Frontier Center of Ministry of Education (NFC-MOE) & Collaborative Innovation Center of Quantum Matter, Peking University, Beijing, 100871, China
[c.] Collaborative Innovation Center of Extreme Optics, Shanxi University, Taiyuan, Shanxi 030006, China

## S1. Waveguide mode analysis of the CQD strip

The cross-section schematic of the CQD strip waveguide is displayed in **Fig. S1**a. The width and height of the CQD strip are $w$ and $h$, respectively. In the simulation, the refractive indexes of the $MgF_2$, PMMA, CQDs, and air are $n$ = 1.38, 1.5, 1.95, and 1.0, respectively. Here, the $MgF_2$ is chose as the transparent substrate for its low refractive index ($n \approx 1.38$), which is beneficial for the better field confinement of the waveguide mode in the CQD strip. When the height of the CQD strip is fixed to be $h$ = 300 nm, the calculated effective refractive indexes ($n_{eff}$) of the waveguide modes ($\lambda$ = 630 nm) supported by the CQD strip with different widths are displayed by the solid lines in Fig. S1b. It is observed that only the fundamental transverse electric ($TE_0$) and transverse magnetic ($TM_0$) modes are supported in the CQD strip when $w$ = $h$ = 300 nm. When the lateral dimension of the CQD strip increases, more waveguide modes are supported. The experiment results (SEM image in Fig. 2B) show that there is a thin CQD layer ($t \approx 60$ nm) on the PMMA film, and the cross-section schematic of the real waveguide is shown in Fig. S1c, where the edges of CQD layer are rounded according to the SEM images in Fig. 2B and Fig. 3C. The calculated effective refractive indexes ($n_{eff}$) of the modes supported by the real waveguide (Fig. S1c) are displayed by the symbols in Fig. S1b. The field ($|E|^2$) and

electric field vector distributions of the $TE_0$ waveguide mode without and with the thin CQD layer ($t \approx 60$ nm) on the PMMA film are displayed by the left and right panels in Fig. S1d, respectively. From Fig. S1b and S1d, it is observed that the thin CQD layer ($t \approx 60$ nm) has little influence on the $TE_0$ waveguide mode in the CQD strip waveguide. The reason is that the field of the $TE_0$ waveguide mode is well confined in the CQD strip, as shown by Fig. S1d. Hence, the small thickness variation (~17% over an area of about1 $cm^2$) brought by the drop-casting technique in the experiment has little influence on the performance of the CQDs-based nanophotonic devices. This is a great advantage in our simple pattern-assisted stacking fabrication approach, and the removal of the CQD layer on the PMMA film is avoided.

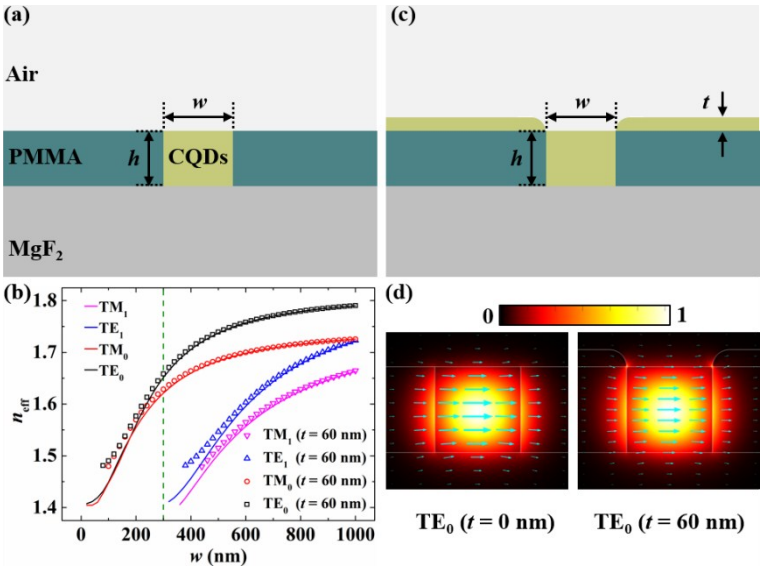


**Fig. S1.** Waveguide modes supported by the CQD strip. (a) Cross-section schematic of the CQD strip waveguide. (b) Calculated effective refractive indexes of the waveguide modes supported by the CQD strip without and with the thin CQD layer ($t \approx 60$ nm) on the PMMA film. (c) Cross-section schematic of the CQD strip waveguide with a thin CQD layer ($t \approx 60$ nm) on the PMMA film. (d) Field ($|E|^2$) and electric field vector distributions of the $TE_0$ waveguide mode (left panel) without and (right panel) with the thin CQD layer ($t \approx 60$ nm) on the PMMA film. The width and height of the CQD strip are $w = h = 300$ nm.

**S2. Propagation length and optimum bending radius of the CQD waveguide**

Based on the pattern-assisted stacking approach, the straight and bending CQD waveguides are fabricated in the experiment. The measured lateral dimension of the CQD strip is about $h$ = 310 nm and $w$ = 290 nm. **Fig. S2**a shows the dark-field optical image of the straight CQD waveguide. The length of the CQD waveguide is about $L$ = 50 μm, and the periods of the gratings at both ends of the waveguide are about 400 nm. The measurements are carried out by a home-made microscope system. When the TE-polarized (electric field vectors perpendicular to the waveguide) beam ($\lambda$ = 630 nm) is focused at the left grating by an objective (100×, NA0.8), the scattered light from the structure is collected by the same objective, and the optical image is displayed in Fig. S2b. The obvious scattered light can be observed at the right grating. Due to the polarization match, only the fundamental $TE_0$ mode (Fig. S1d) is excited in the CQD waveguide. Furthermore, the CQD waveguides with different lengths ($L$) are fabricated, and Fig. S2c shows the measured intensities [ln($I$)] of the scattered light from the right gratings of the CQD waveguides with different lengths. Based on the linear fitting of the scattering intensity and the waveguide length (red line in Fig. S2c),[29] the propagation length of the $TE_0$ mode is calculated to be about $L_p$ = 28.0 μm. This small propagation length is attributed to the absorption loss of the CQD waveguide at $\lambda$ = 630 nm, which can be verified by the absorption spectrum of the CQDs (inset in Fig. S5a). Owing to the absorption of the CQDs in the strip waveguide at $\lambda$ = 630 nm, the fluorescence background can be observed along the CQD waveguide, as shown in Fig. S2b. The measured intensity of the fluorescence along a longer CQD waveguide ($L$ = 150 μm) is depicted by the black line in Fig. S2d. By exponentially fitting the fluorescence intensity along the CQD waveguide (red line in Fig. S2d), the propagation length of the $TE_0$ mode is calculated to be about $L_p$ = 24.9 μm, which is close to that ($L_p$ = 28.0 μm) in Fig. S2c. Moreover, the experimental results show that the propagation length can reach

one millimeter at $\lambda$ = 800 nm, under which the CQD waveguides have less absorption losses (see black line in Fig. S5a).

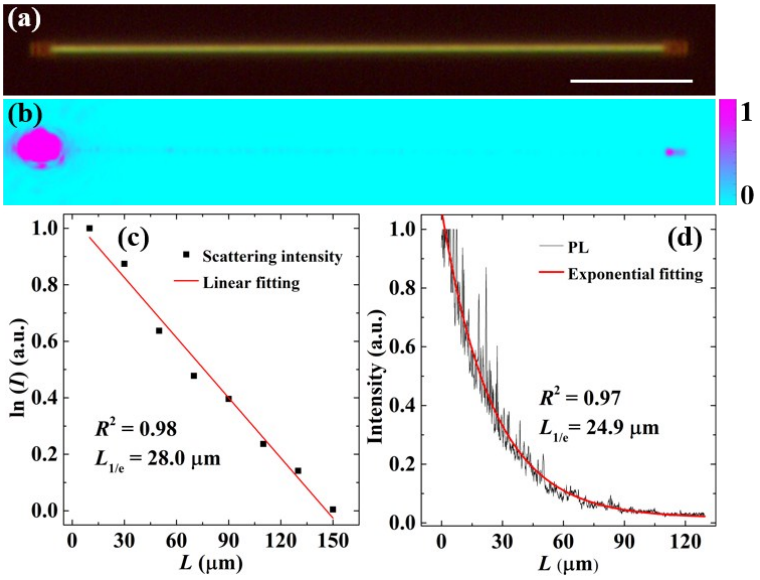


**Fig. S2.** Propagation length of the $TE_0$ mode in the straight CQD waveguide. (a) Dark-field optical image of the CQD waveguide. The scale bar is 10 μm. (b) Optical image of the CQD waveguide when the TE-polarized beam is focused at the left grating. (c) Measured intensities of the scattered light from the right gratings of the CQD waveguides with different lengths. The red line is the linear fitting curve. (d) Measured intensity of the fluorescence along the CQD waveguide. The red line is the exponential fitting curve.

**Fig. S3**a shows the dark-field optical image of the bending CQD waveguide. The bending radius of the bending waveguide is about $R$ = 30 μm, and the lengths of the straight waveguides at both ends of the bending waveguide are about $L$ = 10 μm. When the TE-polarized beam is focused at the lower grating of the bending waveguide, the obvious scattered light is observed at the upper grating, as shown in Fig. S3b. The bending CQD waveguides with different bending radii are also fabricated. The inset of Fig. S3b shows the measured intensities of the scattered light from the upper gratings of the bending waveguides with different bending radii. It is observed that the optimum bending radius is about $R_{opt}$ = 30 μm. The reason is that the bending

loss in the bending CQD waveguide is determined by both the absorption loss and radiation loss of the bending CQD waveguide. The absorption loss is exponentially proportional to the wavelength length (or bending radius), and the radiation loss decreases with the increase the bending radius. Hence, when the bending radius is small, the bending loss is dominated by the radiation loss, and the transmittance increases with the increase of the bending radius, as shown by the inset in Fig. S3b. When the bending radius becomes large, the bending loss is dominated by the absorption loss, and the transmittance decreases with the increase of the bending radius, as shown by the inset in Fig. S3b. Therefore, the optimum bending radius of $R_{opt}$ = 30 μm is attributed to the trade-off between the radiation loss and the absorption loss in the bending CQD waveguide.[30]

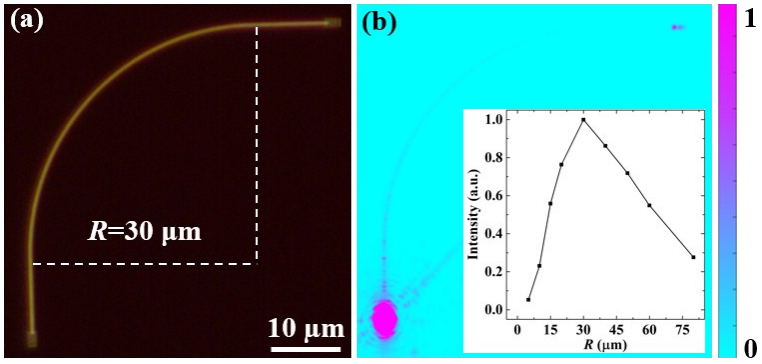


**Fig. S3.** Optimum bending radius of the bending CQD waveguide. (a) Dark-field optical image of the bending CQD waveguide. (b) Optical image of the CQD waveguide when the TE-polarized beam is focused at the lower grating. The inset shows the measured intensities of the scattered light from the upper gratings of the bending CQD waveguides with different radii.

## S3. Lasing from the CQD WRR

The dependence of the peak intensity and linewidth (FWHM) on the pump fluence for the strongest resonant peak ($\lambda$ = 634.8 nm) are depicted by the black square and red circular symbols in Fig. S4a, respectively. It is observed that the peak intensity shows a clear pump threshold ($P_{th} \approx 82$ μJ cm$^{-2}$), and the linewidth exhibits an obvious narrowing from $\Delta\lambda \approx 50$ nm to $\Delta\lambda \approx$

0.4 nm, revealing the occurrence of the lasing in the CQD WRR. In order to measure the polarization of the lasing emission from the CQD WRR, a linear polarizer is inserted in front of the coupling fiber of the spectrometer or the CMOS camera. The measured lasing intensities under different angles of the polarizer are displayed by the black square symbols in **Fig. S4**b. It is observed that the lasing polarization is along the corresponding radial direction of the CQD WRR, as indicated by the blue dashed line in Fig. S4b. Fig. S4c-f show the optical images of the CQD WRR under different angles of the polarizer (indicted by the black arrows), which also verifies the above analysis. This phenomenon is attributed to that the TE resonant mode dominates the resonance in the CQD WRR, whose quality factor is about 17 times that of the TM resonant mode around $\lambda$ = 630 nm. Fig. S4g shows the simulated field ($|E|^2$) and electric field vector distributions of the TE resonant mode ($\lambda$ = 630.8 nm) in the CQD WRR. It is observed that the TE resonant mode is well confined in the CQD strip (confinement factor[21] $\Gamma$ ≈ 88%) and the electric field vectors are mainly parallel to the substrate surface.

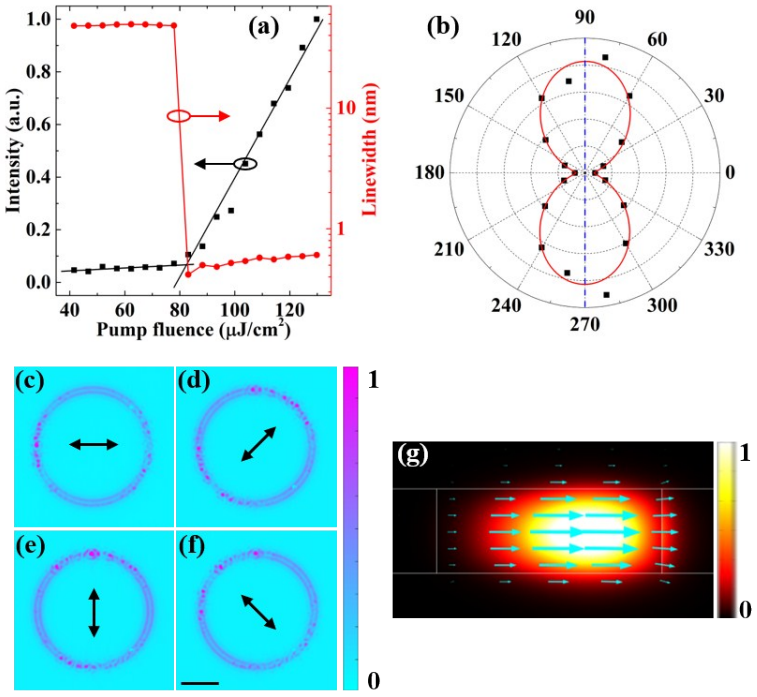


**Fig. S4.** Lasing from the CQD WRR. (a) Dependence of the peak intensity and linewidth on the pump fluence for the strongest resonant peak ($\lambda$ = 634.8 nm). The black lines are the linear

fitting curves. (b) Polarization-dependent lasing intensities from the lowest point of the CQD WRR. The red solid line is the fitting curve, and the blue dashed line indicates the corresponding radial direction of the CQD WRR. (c-f) Optical images of the CQD WRR under different angles of the polarizer. The scale bar in (f) is 5 μm. (g) Simulated field ($|E|^2$) and electric field vector distributions of the TE resonant mode ($\lambda$ = 630.8 nm) supported by the CQD WRR.

**S4. Optical properties of the CQDs**

The measured absorption and PL spectra of the CQDs dispersed in chloroform are displayed by the black and red lines in **Fig. S5**a, respectively. It is observed that the CQDs have a strong absorption at the wavelength ($\lambda_p$ = 430 nm) of the picosecond pump laser, and the fluorescence of the CQDs locates at $\lambda_c \approx$ 650 nm with a FWHM ≈ 50 nm. According to the zoomed-in absorption spectrum of the CQDs (inset in Fig. S5a), the CQDs exhibit absorption at the wavelengths below 660 nm. The amplified spontaneous emission (ASE) of the CQD film (thickness ≈ 400 nm) on the glass substrate is also measured by a stripe pumping configuration,[9] and the emission spectra under different pump fluences are shown in Fig. S5b. Herein, the length of the strip pump beam is about 2.3 mm. With the increase of the pump fluence, an obvious narrow peak appears in the broadband fluorescence spectrum, which indicates the occurrence of the ASE. The pump threshold of the ASE is measured to be $P_{th} \approx 265$ μJ cm$^{-2}$, as determined by the kink in the linear fitting curves of the ASE intensities under different pump fluences (inset in Fig. S5b). It should be pointed out that the pump threshold will increase if the thickness of the CQD film and the length of the pump beam decrease. The increase of the refractive index of the substrate will also increase the pump threshold. Since the ASE peak is blue-shifted by 17 nm as compared to the fluorescence peak, the CQDs belong to the quasi-type-II CQDs.[21] Based on the ASE spectrum, the gain peak of the CQDs is at $\lambda \approx$ 633 nm, and the gain range (FWHM) of the CQDs is about 13 nm.

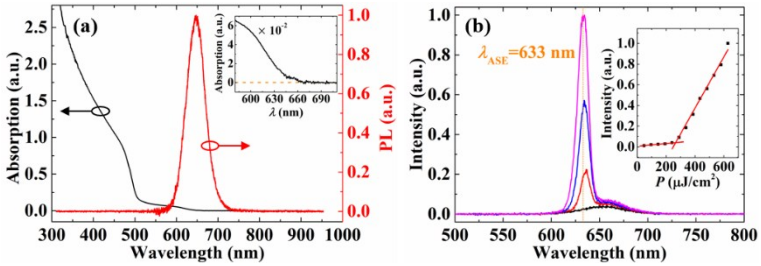


**Fig. S5.** Optical properties of the CQDs. (a) Absorption and PL spectra of the CQDs. The inset shows the zoomed-in absorption spectrum of the CQDs around $\lambda = 630$ nm. (b) Emission spectra of the CQD film under different pump fluences. The inset shows the ASE intensities under different pump fluences, and the red lines are the linear fitting curves.

## S5. Lasing action in the coupling structure

Under different pump fluences, the emission spectra of the CQD WRR coupled with a straight waveguide are displayed in **Fig. S6**a. With the increase of the pump fluence, several narrow resonant peaks are observed in the broadband fluorescence spectrum of the CQDs. The peak intensities and linewidths of one resonant peak ($\lambda \approx 631.5$ nm) under different pump fluences are depicted by the black square and red circular symbols in Fig. S6b, respectively. From Fig. S6b, a clear pump threshold ($P_{th} \approx 100$ μJ cm$^{-2}$) and an obvious linewidth narrowing (from $\Delta\lambda \approx 50$ nm to $\Delta\lambda \approx 0.4$ nm) are observed, indicating the occurrence of the lasing in the CQD WRR coupled with a straight waveguide. The optical images of the coupling structure below ($0.7P_{th}$) and above ($1.3P_{th}$) the pump threshold are displayed in Fig. S6c and d, respectively. The lasing emission in the CQD WRR is coupled to the CQD waveguide, and the gratings at both ends of the waveguide become very bright (Fig. S6d). More importantly, the intensities of the scattered light from the left grating ($I_L$) and the right grating ($I_R$) are nearly the same ($I_L : I_R \approx 0.93 : 1$).

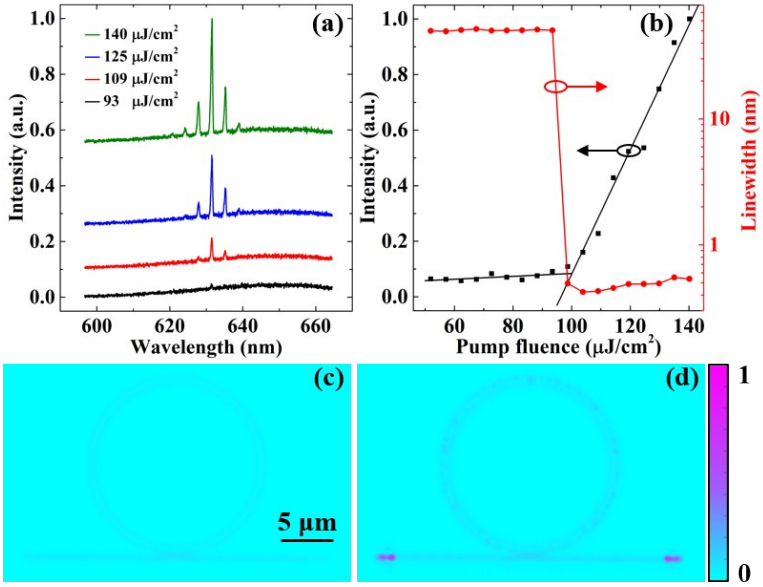


**Fig. S6.** Lasing action in the coupling structure. (a) Emission spectra of the CQD WRR under different pump fluences. (b) Dependence of the peak intensity and linewidth on the pump fluence for the strongest resonant peak. The black lines are the linear fitting curves. Optical images of the coupling structure (c) below and (d) above the pump threshold. The exposure time of the CMOS camera is intentionally decreased to make the scattered light from the gratings under saturation.

**S6. Structural parameters and lasing spectra of various complicated coupling structures**

The schematic of the CQD Y-splitter is depicted by the red part in **Fig. S7**a. The length and channel separation of the Y-splitter are $W$ = 12 μm and of $H$ = 2 μm, respectively. At the three ports of the Y-splitter, there are straight CQD waveguides. The lengths of the straight waveguides are also depicted in Fig. S7a. Fig. S7b shows the zoomed-in dark-field optical image of the Y-splitter (the same one in Fig. 5A), in which the smooth scattered light can be observed. Under the pump beam (spot diameter $\Phi \approx$ 80 μm and fluence $P \approx$ 165 μJ cm$^{-2}$), the measured single-mode lasing wavelengths ($\lambda \approx$ 629.3 nm) of the scattered light from the three positions (B, C, and D) are the same as that from the single-mode laser (position A), as shown in Fig. S7c. This phenomenon further verifies that the single-mode laser in the coupled WRRs

has been successfully routed to the Y-splitter. The MZ interferometer is composed of two consecutive Y-splitters, as shown by the red parts in Fig. S7d. Herein, two straight waveguides with lengths of 2 μm are inserted between the two Y-splitters. Fig. S7e shows the zoomed-in dark-field optical image of the MZ interferometer (the same one in Fig. 5C), in which the smooth scattered light can also be observed. Under the pump beam ($\Phi \approx 80$ μm and $P \approx 192$ μJ cm$^{-2}$), the same single-mode lasing wavelength ($\lambda \approx 630.2$ nm) of the scattered light from the coupled WRRs (position I) and the two ends of the MZ interferometer (position II and III) is also observed (Fig. S7f), further confirming that the single-mode laser in the coupled WRRs has been routed to the MZ interferometer.

Furthermore, a more complex coupling structure, which comprises one CQD WRR laser, one MZ interferometer, one Y-splitter, two straight waveguides, two bending waveguides, and five gratings, is fabricated by the proposed pattern-assisted stacking approach. The schematic and structural parameters of this coupling structure are depicted in Fig. S7g. The pump threshold of the CQD WRR laser is about $P_{th} = 180$ μJ cm$^{-2}$. The lasing signals from the CQD WRR laser can be coupled to the integrated photonic devices (MZ interferometer, Y-splitter, straight waveguide, bending waveguide, and grating). The spectra of the scattered light from the gratings (position P1, P2, P3, P4, and P5) and the CQD WRR (position P6) are measured under the pump fluence of $P \approx 260$ μJ cm$^{-2}$, and the results are displayed in Fig. S7h. It is observed that the lasing wavelengths of the spectra at the six positions (P1, P2, P3, P4, P5, and P6) are the same, strongly confirming that the scattered light from the gratings is coupled from the CQD WRR laser.

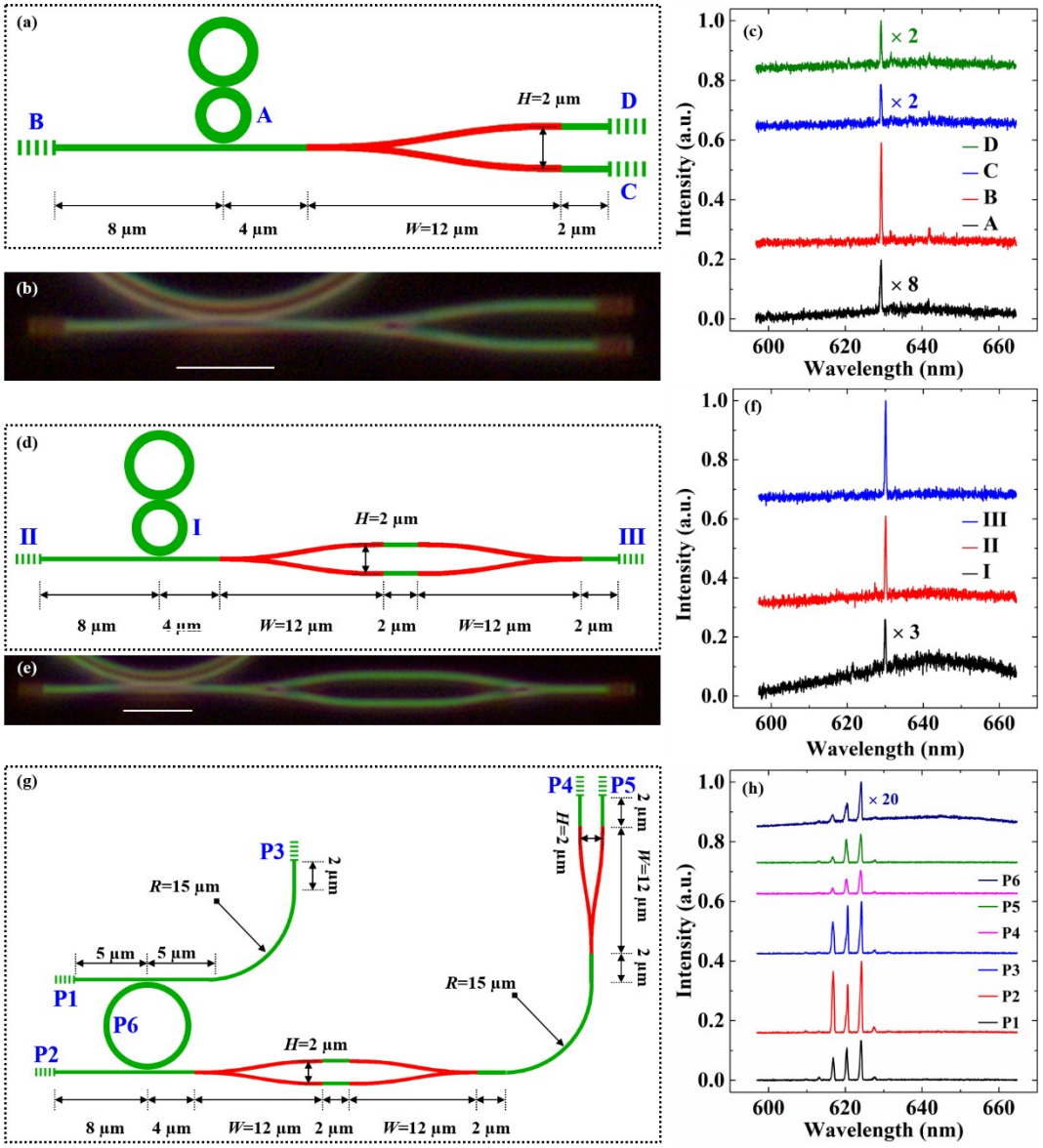


**Fig. S7.** Structural parameters and lasing spectra of various complicated coupling structures. (a) Schematic and structural parameters of the Y-splitter. (b) Zoomed-in dark-field optical image of the Y-splitter. The scale bar is 5 μm. (c) Spectra of the scattered light from different positions of the coupling structure with the Y-splitter. (d) Schematic and structural parameters of the MZ interferometer. (e) Zoomed-in dark-field optical image of the MZ interferometer. The scale bar is 5 μm. (f) Spectra of the scattered light from different positions of the coupling structure with the MZ interferometer. (g) Schematic and structural parameters of the more complex coupling structure. (h) Spectra of the scattered light from different positions of the more complex coupling structure.

**S7. Low-noise optical amplification**

The schematic and structural parameters of the coupling structure with unequal waveguide lengths at the left and right sides of the CQD WRR are depicted in **Fig. S8**a. Under the pump beam ($\Phi \approx 17$ μm and $P \approx 1.5P_{th}$), the measured spectra of the scattered light from the left and right gratings are depicted by the black and red lines in Fig. S8b, respectively. Due to the larger absorption loss in the long right CQD waveguide ($L_R \approx 40$ μm >> $L_L \approx 15$ μm), all the lasing signals at the right grating are attenuated as compared to that at the left grating. The upper panel of Fig. S8c shows the zoomed-in spontaneous emission backgrounds (noises) in Fig. S8b. It is clearly observed that both the spontaneous emission noises from the left and right gratings are nearly the same (approaching zero), and the calculated signal-to-noise ratio is as high as S/N ≈ 250. When the spot diameter increases to be $\Phi \approx 80$ μm, the zoomed-in spontaneous emission backgrounds (Fig. 6D) are displayed in the lower panel of Fig. S8c. Although the lasing signals at the right grating are much greater than that at the left grating (indicating the amplification of the lasing signals), both the spontaneous emission noises from the two gratings are still nearly the same (approaching zero). The calculated signal-to-noise ratio is as high as S/N ≈ 300. Since the size of the coupling structure (15 μm × 55 μm) is much smaller than that ($\Phi \approx 80$ μm) of the pump spot, the CQD waveguide is assumed to be uniformly pumped. For a lasing signal [intensity of $I_0(\lambda)$] in the CQD WRR, the scattered intensities of the lasing signal at the left and right gratings satisfy $I_L(\lambda) = I_0(\lambda)\eta_0(\lambda)\eta_1(\lambda)\exp[g(\lambda)L_L]$ and $I_R(\lambda) = I_0(\lambda)\eta_0(\lambda)\eta_1(\lambda)\exp[g(\lambda)L_R]$, respectively. Here, $\eta_0(\lambda)$ is the coupling efficiency from the WRR to the waveguide, and $\eta_1(\lambda)$ is the scattering efficiency of the grating. Hence, the net gain coefficient $g(\lambda)$ of the lasing signal is deduced to be

$$g(\lambda) = \ln[I_R(\lambda)/I_L(\lambda)]/(L_R - L_L). \quad (1)$$

Herein, the positive and negative signs of the $g(\lambda)$ value denote the gain and loss, respectively. In the calculations, the scattered intensity of the lasing signal is obtained by multiplying the scattering intensity of the grating (optical image in Fig. 6C) with the relative intensity of the lasing signal (spectra in Fig. 6D). Based on **Equation 1**, the calculated net gain coefficients of one lasing signal ($\lambda$ = 632.2 nm) under different pump fluences ($1.2P_{th}$–$2.0P_{th}$) are depicted in Fig. S8d. With the increase of the pump fluence, it is observed that the net gain coefficient shows a gradual increase, and it reaches a value greater than $g$ = 600 cm$^{-1}$ (2600 dB cm$^{-1}$) at $P$ = $2.0P_{th}$.

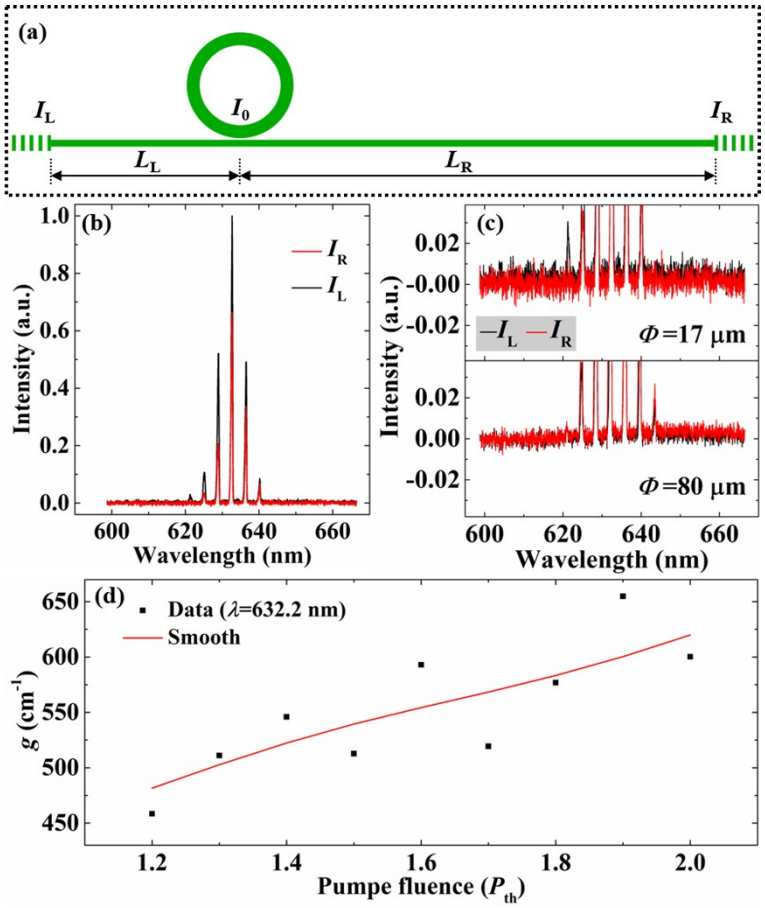


**Fig. S8.** Low-noise optical amplification in the CQD waveguide. (a) Schematic and structural parameters of the coupling structure. (b) Measured spectra of the scattered light from the left and right gratings when the spot diameter of the pump beam is about $\Phi$ = 17 μm. (c) Zoomed-in spontaneous emission backgrounds when the spot diameters are about (upper panel) $\Phi$ = 17

μm and (lower panel) $\Phi$ = 80 μm. (d) Calculated net gain coefficients of one lasing mode ($\lambda$ = 632.2 nm) under different pump fluences. The red line is the smooth result.